










The microstructure of non-polar a-plane (11 $\bar{2}$ 0) InGaN quantum wells

Cite as: J. Appl. Phys. **119**, 175703 (2016); <https://doi.org/10.1063/1.4948299>

Submitted: 19 February 2016 . Accepted: 15 April 2016 . Published Online: 02 May 2016

 James T. Griffiths,  Fabrice Oehler, Fengzai Tang, Siyuan Zhang,  Wai Yuen Fu,  Tongtong Zhu,  Scott D. Findlay, Changlin Zheng,  Joanne Etheridge,  Tomas L. Martin, Paul A. J. Bagot, Micheal P. Moody, Danny Sutherland,  Philip Dawson, Menno J. Kappers,  Colin J. Humphreys, and  Rachel A. Oliver



View Online



Export Citation



CrossMark

ARTICLES YOU MAY BE INTERESTED IN

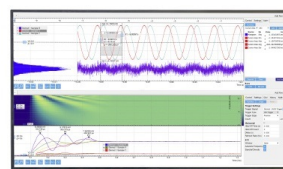
[Indium clustering in a-plane InGaN quantum wells as evidenced by atom probe tomography](#)
Applied Physics Letters **106**, 072104 (2015); <https://doi.org/10.1063/1.4909514>

[Three-dimensional atom probe studies of an \$\text{In}_x\text{Ga}_{1-x}\text{N}\$ / GaN multiple quantum well structure: Assessment of possible indium clustering](#)
Applied Physics Letters **90**, 061903 (2007); <https://doi.org/10.1063/1.2431573>

[Band parameters for nitrogen-containing semiconductors](#)
Journal of Applied Physics **94**, 3675 (2003); <https://doi.org/10.1063/1.1600519>

Challenge us.

What are your needs for
periodic signal detection?



Zurich
Instruments

The microstructure of non-polar a-plane (11 $\bar{2}$ 0) InGaN quantum wells

James T. Griffiths,¹ Fabrice Oehler,^{1,2} Fengzai Tang,¹ Siyuan Zhang,¹ Wai Yuen Fu,¹ Tongtong Zhu,¹ Scott D. Findlay,³ Changlin Zheng,⁴ Joanne Etheridge,^{4,5} Tomas L. Martin,⁶ Paul A. J. Bagot,⁶ Micheal P. Moody,⁶ Danny Sutherland,⁷ Philip Dawson,⁷ Menno J. Kappers,¹ Colin J. Humphreys,¹ and Rachel A. Oliver¹

¹Department of Materials Science and Metallurgy, University of Cambridge, Cambridge CB3 0FS, United Kingdom

²Laboratoire de Photoniques et Nanostructures, CNRS/LPN, Route de Nozay, Marcoussis, France

³School of Physics and Astronomy, Monash University, Victoria 3800, Australia

⁴Monash Centre for Electron Microscopy, Monash University, Victoria 3800, Australia

⁵Department of Materials Science and Engineering, Monash University, Victoria 3800, Australia

⁶Department of Materials, University of Oxford, Parks Road, Oxford OX1 3PH, United Kingdom

⁷School of Physics and Astronomy, Photon Science Institute, University of Manchester, Manchester M13 9PL, United Kingdom

(Received 19 February 2016; accepted 15 April 2016; published online 2 May 2016)

Atom probe tomography and quantitative scanning transmission electron microscopy are used to assess the composition of non-polar a-plane (11-20) InGaN quantum wells for applications in optoelectronics. The average quantum well composition measured by atom probe tomography and quantitative scanning transmission electron microscopy quantitatively agrees with measurements by X-ray diffraction. Atom probe tomography is further applied to study the distribution of indium atoms in non-polar a-plane (11-20) InGaN quantum wells. An inhomogeneous indium distribution is observed by frequency distribution analysis of the atom probe tomography measurements. The optical properties of non-polar (11-20) InGaN quantum wells with indium compositions varying from 7.9% to 20.6% are studied. In contrast to non-polar m-plane (1-100) InGaN quantum wells, the non-polar a-plane (11-20) InGaN quantum wells emit at longer emission wavelengths at the equivalent indium composition. The non-polar a-plane (11-20) quantum wells also show broader spectral linewidths. The longer emission wavelengths and broader spectral linewidths may be related to the observed inhomogeneous indium distribution. © 2016 Author(s). All article content, except where otherwise noted, is licensed under a Creative Commons Attribution (CC BY) license (<http://creativecommons.org/licenses/by/4.0/>). [<http://dx.doi.org/10.1063/1.4948299>]

I. INTRODUCTION

Blue In_xGa_(1-x)N quantum well (QW) based light emitting diodes (LEDs) exhibit high efficiencies compared to traditional lighting sources.^{1,2} However, the efficiency of nitride devices rapidly decreases at longer emission wavelengths, which extend into the green spectrum.³⁻⁶ Emission over the green spectral region is particularly important for lighting and display technologies since it is where the response of the human eye is greatest. The development of longer wavelength devices, though, is in part inhibited by the strong polarization fields in conventional polar structures.⁷⁻¹¹ As the indium composition is increased to achieve longer wavelength emission, the stronger polarization field leads to greater separation of the electron and hole wavefunctions and a reduction in the radiative recombination efficiency. However, growth along non-polar orientations suppresses the internal electric field along the growth axis^{12,13} and hence may aid in the development of high efficiency longer wavelength emission devices.

The distribution of indium in the quantum wells also affects the emission wavelength. Indium rich regions may serve as deep energy potentials, which act as localization centers for carriers and affect the spectral characteristics.¹⁴⁻¹⁹ It has been widely reported that polar (0001) InGaN QW structures exhibit a random indium distribution,^{20,21} which has also been observed by Riley *et al.* in

non-polar m-plane (1-100) InGaN QWs.²² However, Tang *et al.* have recently suggested that non-polar a-plane (11-20) QWs may exhibit an inhomogeneous distribution of indium.²³ The non-random distribution of indium may have important consequences for the peak emission wavelength as well as the spectral linewidth.²⁴

Here, we investigate different approaches to measure the alloy composition profile in non-polar a-plane (11-20) InGaN QWs. The non-polar QWs are grown on GaN ammonothermal substrates to suppress stacking faults, reduce the dislocation density to $1 \times 10^4 \text{ cm}^{-2}$, and improve the crystal quality.²⁵ The composition of the QWs is measured by both atom probe tomography (APT) and quantitative scanning transmission electron microscopy (Q-STEM). The average composition measurements are also compared with X-ray diffraction (XRD). Furthermore, APT is applied to study non-uniformities in the indium distribution in the QWs. We proceed to measure the photoluminescence (PL) spectral properties of the non-polar a-plane (11-20) QWs over a range of indium compositions, and compare with QWs grown on the perpendicular non-polar m-plane (1-100).

II. SAMPLE DETAILS

Four non-polar a-plane (11-20) samples were grown by metal organic vapor phase epitaxy (MOVPE) in a Thomas

Swan 6×2 -in. close-coupled showerhead reactor. For reference, four non-polar m-plane (1–100) samples were also grown by MOVPE. Trimethylgallium (TMG), trimethylindium (TMI), and ammonia were used as the precursors with hydrogen as the carrier gas for the growth of the GaN epilayer and nitrogen for the growth of InGaN QWs and GaN barrier layers. All of the samples were grown on ammonothermal GaN substrates with a miscut of $0.3 \pm 0.20^\circ$ towards [0001] for the non-polar a-plane (11–20) and $2.0 \pm 0.20^\circ$ towards [000–1] for the non-polar m-plane (1–100). An 800 nm non-intentionally doped GaN epilayer was grown directly on the substrate. Five-period InGaN/GaN QWs were grown at 300 Torr in a constant ammonia flow of 446 mmol/min. The InGaN QWs were grown for 160 s with a TMI flow of $14.5 \mu\text{mol}/\text{min}$ and a TMG flow of $4.5 \mu\text{mol}/\text{min}$. Following the growth of each InGaN QW, a 1 nm GaN protective layer was grown at the same temperature as the InGaN. The GaN barrier growth continued during the temperature ramp to 860°C over 90 s at which point the TMG flow rate was increased to $73.2 \mu\text{mol}/\text{min}$ with a nominal thickness of 6 nm, following the quasi-two-temperature approach.²⁶ The indium composition of the QWs was varied by changes in the growth temperature between 705°C and 690°C for the non-polar a-plane (11–20) QWs and between 745°C and 705°C for the non-polar m-plane (1–100) QWs.

III. RESULTS AND DISCUSSION

A. Composition analysis of the non-polar (11–20) QWs

The $\text{In}_x\text{Ga}_{(1-x)}\text{N}$ indium composition, defined in this study as the group-III alloy fraction (x), was quantified from atomic resolution STEM images of the a-plane (11–20) QWs grown at 695°C . The Q-STEM approach is taken in this study as it can provide high spatial resolution and chemical sensitivity with a lower electron dose than energy dispersive X-ray spectroscopy (EDS) or electron energy loss spectroscopy (EELS) and has shown no evidence for the formation of indium rich regions or observable damage,²⁷ which have been previously reported.^{20,28,29}

High resolution high angle annular dark field (HAADF) STEM was performed using an FEI Titan³ 80–300 keV Schottky field emission gun TEM fitted with spherical aberration correctors on the probe and image forming lenses. STEM was performed at 300 keV, with a probe convergence semi-angle of 16.2 mrad. The HAADF signal was detected on a Fischione Instruments 3000 ADF detector spanning from 46 mrad to approximately 200 mrad.

For quantitative compositional analysis of the HAADF-STEM images, theoretical HAADF-STEM intensities were simulated for comparison using a frozen phonon multislice model following the approach of Rosenauer *et al.*²⁷ using electron image simulation software adapted from the μSTEM code developed at the University of Melbourne.³⁰ The simulations assumed the same accelerating voltage and probe convergence semi-angle as the experiment, and modeled the aberration-corrected probe as being aberration-free. The thermal motion of the atoms was considered based on the displacement of the atoms according to a Gaussian probability arising from Einstein's simple harmonic oscillator

model.^{31,32} The detector response was recorded by scanning over the whole detector in real space, in the absence of any specimen, with the same brightness and contrast settings used to record the HAADF-STEM images. Image intensity calculations were performed for indium fractions from 0 to 0.24, in steps of 0.04, up to a maximum thickness of 130 nm, incorporating the measured detector response into the simulations. Experiment and simulation were placed on a common scale by normalization of the intensity with respect to the average detector response of the incident electron beam using the expression

$$I = \frac{I_{\text{raw}} - I_{\text{dark}}}{I_{\text{det}} - I_{\text{dark}}},$$

where I is the normalized image intensity, I_{raw} is the raw image intensity, I_{det} is the average detector response, and I_{dark} is the dark intensity.

Static atomic displacements (SADs) due to the difference in the size of the covalent radius of indium and gallium were included as they have been shown to significantly affect the HAADF-STEM intensity.^{33,34} The SADs corresponding to the minimum elastic energy were determined by the LAMMPS molecular dynamics (MD) code,³⁵ using empirical potentials in the Stillinger-Weber parameterization.³⁶

Each of the simulated intensities was averaged over four different supercells, comprising 8×5 unit cells, each with a different SAD and frozen phonon configuration. With four group-III columns for each unit cell, this corresponds to averaging over 640 separate configurations, to achieve a reliable average over different phonon configurations and SADs. The results were interpolated using a cubic polynomial and compiled into a thickness-composition matrix, shown in Figure 1.

Figure 2(a) shows the atomic resolution HAADF-STEM image viewed along [0001]. The position of the atomic columns were found after cross-correlating the raw image with a Gaussian function, and the image was segmented into Voronoi cells for each atomic column position, shown in the

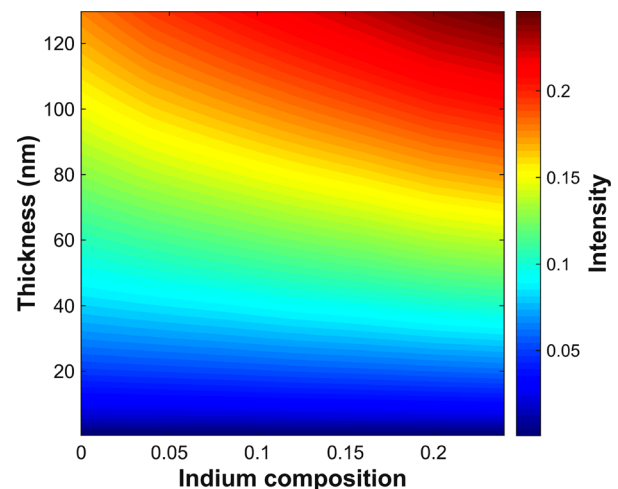


FIG. 1. The theoretical STEM image intensity, normalized with respect to the incident electron beam, for the specimen thickness and the indium composition.

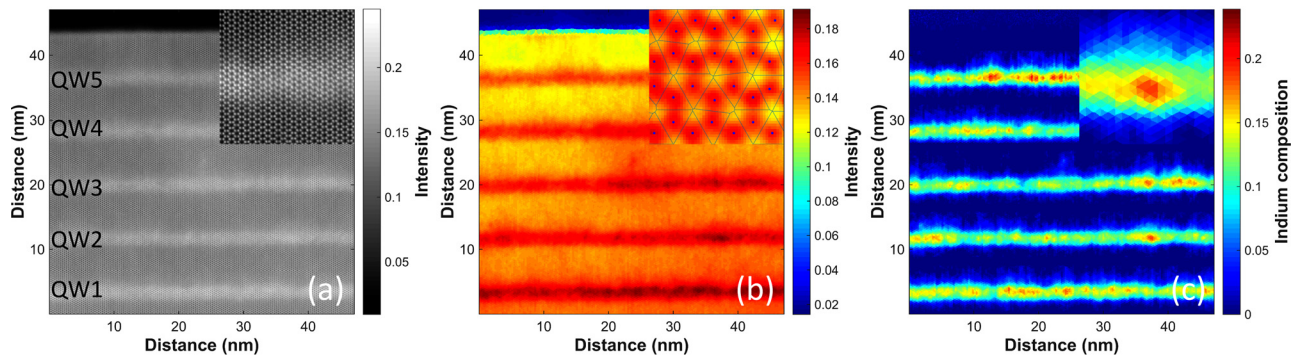


FIG. 2. (a) The recorded HAADF-STEM image of the non-polar a-plane (11-20) InGaN QWs grown at 695 °C shown with bright contrast, and the GaN barriers with dark contrast. (b) The STEM intensity of each atomic column averaged over each unit cell, with the inset showing the Gaussian filtered image for atomic column identification (dots) and the corresponding boundary of the atomic column. (c) The distribution of indium, with the inset showing strong local alloy fluctuations.

inset of Figure 2(b). Since the image intensity associated with a given atomic column may contain contributions from neighbouring atomic columns,^{37,38} the mean intensity of the pixels within the Voronoi cell of the raw image was averaged over the adjacent neighbours^{39–41} to produce the intensity map shown in Figure 2(b). Averaging over the adjacent atomic columns has the additional advantage that it makes the results largely independent of coherent aberrations (such as defocus and spherical aberration) as well as spatial and temporal incoherence.⁴² The thickness in the GaN regions between the QWs was determined by quantitative comparison between the intensity map and the thickness-composition matrix. The thickness estimates were extrapolated across the InGaN regions by fitting a fifth order polynomial across the QWs. This thickness information was combined with the integrated intensities in Figure 2(b) and the reference thickness-composition matrix to determine the indium composition shown in Figure 2(c).

APT was carried out in a pulsed laser mode with a pulse energy of 4 pJ with a pulse frequency of 200 kHz on a Cameca LEAP 3000XHR with a detector efficiency of 37% on the same a-plane (11-20) sample studied by Q-STEM. The analysis was performed at 30 K, with an average detection rate of 0.005 ions per pulse. Reconstructions were performed using the IVAS software package CAMECA, in which the thickness of the QW and GaN barrier measured by STEM were used for reference. Figure 3 shows an APT reconstruction of the indium atom distribution across the 5 QWs in a 50 nm cube of the non-polar a-plane (11-20) InGaN QWs grown at 695 °C, with 50% of the reconstructed indium atoms shown.

Figure 4 shows the indium composition profile of the QWs, along the growth direction determined by APT and Q-STEM, along with the average composition determined by XRD. The APT and Q-STEM indium profiles reflect variations in the composition between QWs and the composition profile across each QW. The APT and Q-STEM composition profiles show a tail of indium at the upper interface, extending into the GaN barrier. A comparison of the fifth QW with a symmetric Gaussian shown in Figure 4(b) highlights the asymmetric indium distribution across the QWs in the non-polar (11-20) InGaN QWs. A tail of indium at the upper

surface has also been observed in the polar InGaN QWs.^{43–46} Chen *et al.* have previously shown that in the polar InGaN QWs the indium is not fully incorporated during growth leading to the presence of an indium-rich floating layer at the surface.⁴⁷ The indium-rich floating layer is then gradually incorporated into the GaN barrier leading to the observed asymmetric indium distribution profile. This is also expected to occur in the non-polar structures due to the reduced indium incorporation in the non-polar structures.⁴⁸

The peak indium compositions measured by APT vary from 16.4% (QW1) to 14.5% (QW5) and shows that the first QW is substantially richer in indium relative to the following QWs. The peak indium compositions measured by Q-STEM also show that the first QW is richer in indium varying from 13.9% (QW1) to 12.4% (QW5). The higher indium composition of the first QW has also been previously observed in the more established polar (0001) InGaN QWs.⁴⁹ Comparison between the APT and Q-STEM shows variations in the peak indium composition of less than 3.1%, which is also similar to the differences observed by Mehrrens *et al.*⁵⁰ The discrepancy here may also be in part due to variations in the indium distribution across the wafer although steps were taken to minimize this impact.

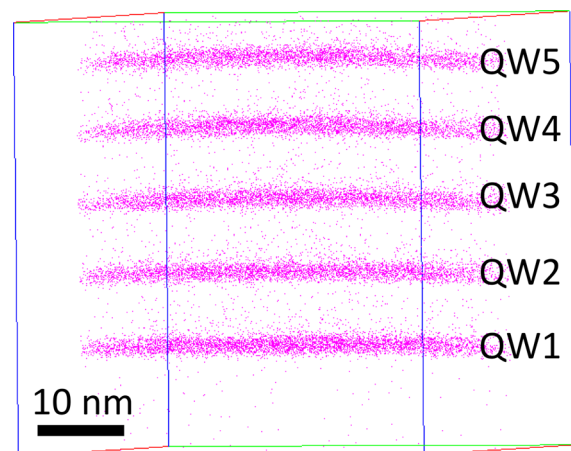


FIG. 3. A 3D APT reconstruction over a 50 nm cube of the non-polar a-plane (11-20) InGaN QWs grown at 695 °C, with 50% of the detected indium atoms shown for clarity.

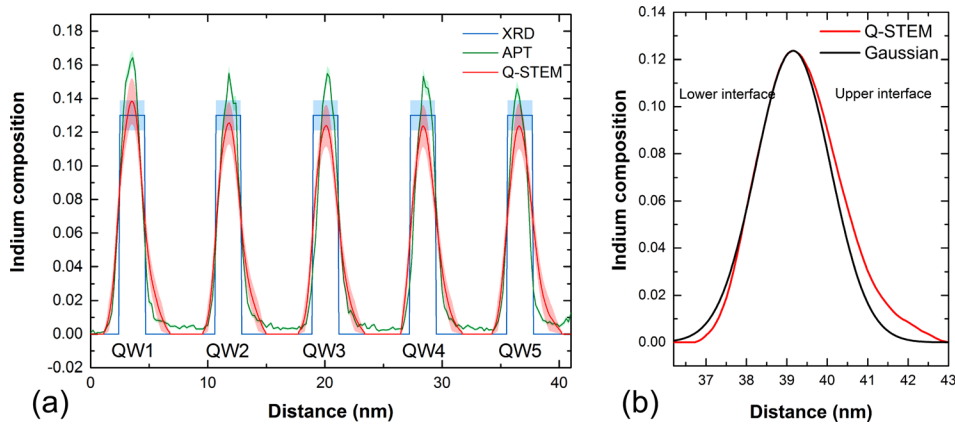


FIG. 4. (a) Composition line profile of the indium composition along the [11-20] growth direction determined by APT, Q-STEM, and XRD. (b) The composition profile measured by Q-STEM of QW5, compared with a Gaussian distribution. The Q-STEM profile shows an asymmetric distribution of indium with a tail of indium extending into the GaN barrier.

XRD is a rapid, non-destructive and widely used technique to measure the indium composition. Here, we compare the average indium compositions measured by XRD with those measured by APT and Q-STEM. High resolution XRD was performed on a Philips X'pert MRD diffractometer with a 4-bounce monochromator and a triple axis analyzer. The QW widths and lattice parameters were determined by ω - 2θ scans performed on the (11-20) reflection for the non-polar (11-20) samples and on the (1-100) reflection for the (1-100) samples following the approach of Vickers *et al.*⁵¹ and its adaptation to non-polar orientations.⁵² XRD however does not reveal variations in the composition between QWs or within the QW, but instead provides an average composition for the QWs. Since the APT and Q-STEM indium profiles show an asymmetric indium distribution across the QWs, for comparison with the XRD measurements the indium composition profile was integrated over the full QW period and normalized to the average FWHM of the QWs. The average indium composition measured by APT was 14.7 ± 0.9 , and by Q-STEM is 13.9 ± 1.6 , compared with 13.0 ± 0.9 alloy percent calculated by XRD, and hence, all three measurement approaches concur on the average indium composition within the experimental errors.

B. Study of the indium distribution

The distribution of indium atoms in the QWs was assessed in the APT data by frequency distribution analysis. The analysis was performed on each QW independently with volumes for analysis defined at the upper and lower interfaces at the FWHM of the indium composition. Analysis was performed with histogram bin sizes ranging from 25 to 200 atoms in increments of 25 atoms, corresponding to volumes with linear dimensions ranging from 1.2 to 2.4 nm. Figure 5 shows the experimentally observed indium distribution of QW1 with a 100 atom bin size, compared with a random binomial arrangement of indium atoms in the QWs. The experimental distribution of indium atoms exhibits significant deviations from the expected random distribution, shown in Figure 5(b). A χ^2 analysis of the data indicates a p -value less than 0.001, indicating no correlation between the experimental data and a random distribution exists. The calculated p -value therefore suggests that the indium atom distribution does not adhere to a random distribution. Analysis on QW1 over all other bin sizes also does not show a random

distribution. The same analysis performed on the following QWs also does not show a random distribution of indium, in agreement with the previous study by Tang *et al.*,²³ but further shows that stacking faults and a high dislocation density are not necessary for the formation of indium rich regions.

C. The optical characteristics of the non-polar a-plane (11-20) InGaN QWs compared with the non-polar m-plane (1-100) InGaN QWs

Whilst XRD may not have the spatial resolution shown by APT or Q-STEM, Sec. III A has shown it as an accurate

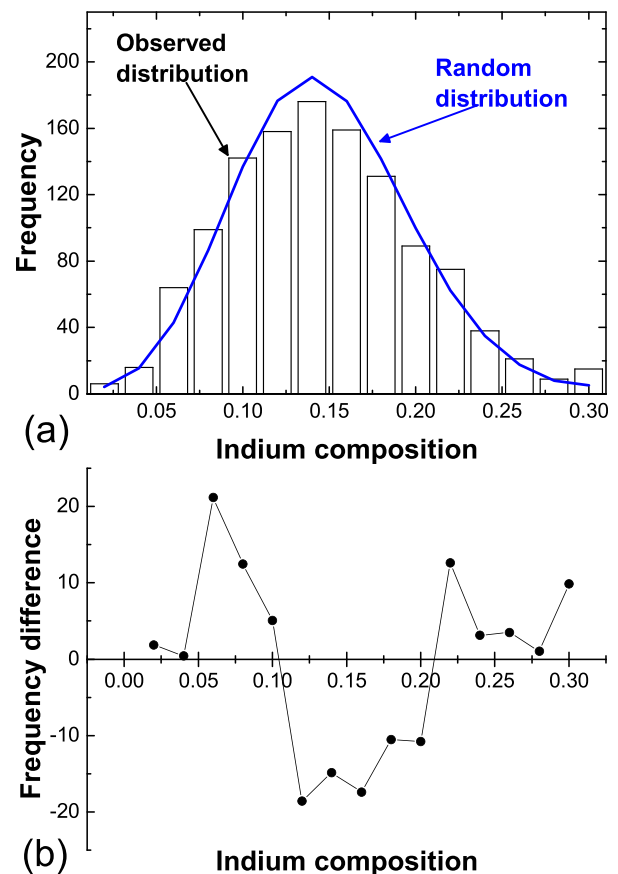


FIG. 5. (a) Frequency distribution analysis of the indium composition in the first QW within 50 atom regions. (b) The frequency difference between the experimental data and a binomial distribution. The frequency difference shows a deviation from a random distribution of indium atoms.

approach to measure the average alloy composition of the QWs. Figure 6 shows the variation in the peak emission wavelength of four non-polar a-plane (11–20) InGaN QWs, including the sample previously characterised by XRD. The PL spectra were measured at 10 K using excitation from a 325 nm HeCd continuous laser. The luminescence was focused onto the slits of an 85 cm single grating spectrometer and detected with a Peltier-cooled GaAs photomultiplier tube. For reference, the variation in the peak emission wavelength with respect to the indium composition of four non-polar m-plane (1–100) InGaN QWs is also shown. The measured peak wavelengths of the non-polar m-plane (1–100) samples are similar to those reported by Masui *et al.* for the m-plane QWs where the indium fraction varied between 0.09 and 0.28.⁵³ The peak wavelengths of the emission from the non-polar a-plane (11–20) QWs occur at longer wavelengths over the entire range compared with the non-polar m-plane (1–100) QWs at the same indium composition. The spectral linewidth of the PL spectra of the non-polar a-plane (11–20) QWs is also broader than the corresponding non-polar m-plane (1–100) QWs. Both the emission wavelength and linewidth of the a-plane (11–20) QWs are longer and broader at the equivalent indium composition, whilst variations in the indium composition between QWs are comparable, and hence, differences in the optical properties may be attributed to alloy fluctuations in the QW. A number of studies have shown that indium alloy fluctuations can serve to localize the carriers and strongly influence the emission

wavelength and the spectral linewidth.^{14–16,54–59} Recently, Schulz *et al.*²⁴ have shown through atomistic tight binding calculations that the spectral properties of non-polar InGaN QWs are dominated by the effects of exciton localization at indium fluctuations and that the indium alloy fluctuations leads to the observed emission wavelengths and broad spectral linewidths. The longer emission wavelengths and the broader spectral linewidths of the non-polar (11–20) InGaN QWs may therefore be indicative of stronger localization of carriers at non-random alloy fluctuations observed in the APT analysis. The stronger alloy fluctuations in the a-plane (11–20) InGaN QWs may arise due to the lower QW growth temperature compared to the m-plane (1–100) InGaN QWs; however, the cause of the behavior is still under investigation.

IV. CONCLUSION

APT and Q-STEM were applied to investigate the composition of non-polar a-plane (11–20) InGaN QWs. Both APT and Q-STEM revealed variations in the compositions between individual QWs as well as an asymmetric indium profile across the QW, with a tail of indium extending into the GaN barrier. This study shows for the first time that the average composition measured by APT and Q-STEM is in quantitative agreement with XRD measurements. The distribution of indium in the non-polar a-plane (11–20) InGaN QWs was investigated by frequency distribution analysis of the APT measurements. Analysis revealed that the indium does not exhibit a random distribution in the QWs in agreement with the previous study by Tang *et al.*²³ The spectral properties of a range of non-polar a-plane (11–20) QWs with varying indium compositions were studied by low temperature PL measurements. The non-polar a-plane (11–20) InGaN QWs were found to emit at longer emission wavelengths at the equivalent indium composition than InGaN QWs on the alternate non-polar m-plane (1–100) orientation. The non-polar a-plane (11–20) QWs also exhibited substantially broader PL linewidths than the non-polar m-plane (1–100) InGaN QWs. The red shift in the emission wavelength and the broader linewidth of the non-polar a-plane (11–20) QWs may be a reflection of the observed deviations from a random alloy distribution.

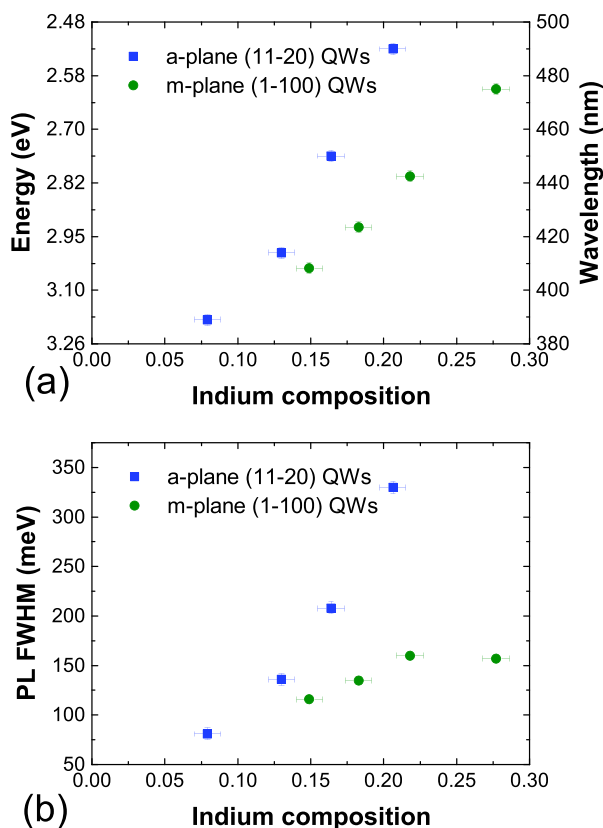


FIG. 6. (a) The variation in the PL emission wavelength at 10 K with respect to the indium composition measured by XRD and (b) the corresponding variation in the PL spectral linewidth with respect to the indium composition for the non-polar a-plane (11-20) QWs and m-plane (1-100) QWs.

ACKNOWLEDGMENTS

This work was carried out with the support of the United Kingdom Engineering and Physical Sciences Research Council under Grants Nos. EPJ001627\1, EP/I012591/1, and EPJ003603\1. The European Research Council has also provided financial support under the European Community's Seventh Framework Programme (FP7/2007-2013)/ERC Grant Agreement No. 279361 (MACONS). J. Etheridge and S. D. Findlay acknowledge funding from the Australian Research Council (ARC) (Project Nos. DP110104734 and DP110101570, respectively). The Titan³ 80-300 TEM/STEM at the Monash Centre for Electron Microscopy was supported by the ARC Grant No. LE0454166. We would like to thank Associate Professor M. Weyland for helpful discussions. Data used in this publication may be accessed at the following link <https://www.repository.cam.ac.uk/handle/1810/255052>.

- ¹Y. Narukawa, M. Ichikawa, D. Sanga, M. Sano, and T. Mukai, *J. Phys. D: Appl. Phys.* **43**, 354002 (2010).
- ²C. J. Humphreys, *MRS Bull.* **33**, 459 (2011).
- ³S. Saito, R. Hashimoto, J. Hwang, and S. Nunoue, *Appl. Phys. Express* **6**, 111004 (2013).
- ⁴T. Mukai, M. Yamada, and S. Nakamura, *Jpn. J. Appl. Phys., Part 1* **38**, 3976 (1999).
- ⁵A. Khan, *Nat. Photonics* **3**, 432 (2009).
- ⁶S. P. DenBaars, D. Feezell, K. Kelchner, S. Pimputkar, C.-C. Pan, C.-C. Yen, S. Tanaka, Y. Zhao, N. Pfaff, R. Farrell, M. Iza, S. Keller, U. Mishra, J. S. Speck, and S. Nakamura, *Acta Mater.* **61**, 945 (2013).
- ⁷D. Miller, D. Chemla, T. Damen, A. Gossard, W. Wiegmann, T. Wood, and C. Burrus, *Phys. Rev. Lett.* **53**, 2173 (1984).
- ⁸F. Bernardini, V. Fiorentini, and D. Vanderbilt, *Phys. Rev. B* **56**, R10024 (1997).
- ⁹V. Fiorentini, F. Bernardini, F. Della Sala, A. Di Carlo, and P. Lugli, *Phys. Rev. B* **60**, 8849 (1999).
- ¹⁰J. T. Griffiths, S. Zhang, B. Rouet-Leduc, W. Y. Fu, A. Bao, D. Zhu, D. J. Wallis, A. Howkins, I. Boyd, D. Stowe, M. J. Kappers, C. J. Humphreys, and R. A. Oliver, *Nano Lett.* **15**, 7639 (2015).
- ¹¹C. Ren, *Mater. Sci. Technol.* **32**(5), 418–433 (2015).
- ¹²J. S. Speck and S. F. Chichibu, *MRS Bull.* **34**, 304 (2011).
- ¹³D. A. B. Miller, D. S. Chemla, T. C. Damen, A. C. Gossard, W. Wiegmann, T. H. Wood, and C. A. Burrus, *Phys. Rev. B* **32**, 1043 (1985).
- ¹⁴S. Chichibu, T. Azuhata, T. Sota, and S. Nakamura, *Appl. Phys. Lett.* **69**, 4188 (1996).
- ¹⁵S. Chichibu, K. Wada, and S. Nakamura, *Appl. Phys. Lett.* **71**, 2346 (1997).
- ¹⁶Y. Narukawa, Y. Kawakami, M. Funato, S. Fujita, S. Fujita, and S. Nakamura, *Appl. Phys. Lett.* **70**, 981 (1997).
- ¹⁷P. R. C. Kent and A. Zunger, *Appl. Phys. Lett.* **79**, 1977 (2001).
- ¹⁸L.-W. Wang, *Phys. Rev. B* **63**, 245107 (2001).
- ¹⁹R. A. Oliver, S. E. Bennett, T. Zhu, D. J. Beesley, M. J. Kappers, D. W. Saxey, A. Cerezo, and C. J. Humphreys, *J. Phys. D: Appl. Phys.* **43**, 354003 (2010).
- ²⁰T. M. Smeeton, M. J. Kappers, J. S. Barnard, M. E. Vickers, and C. J. Humphreys, *Appl. Phys. Lett.* **83**, 5419 (2003).
- ²¹M. J. Galtrey, R. A. Oliver, M. J. Kappers, C. J. Humphreys, D. J. Stokes, P. H. Clifton, and A. Cerezo, *Appl. Phys. Lett.* **90**, 061903 (2007).
- ²²J. R. Riley, T. Detchprohm, C. Wetzel, and L. J. Lauhon, *Appl. Phys. Lett.* **104**, 152102 (2014).
- ²³F. Tang, T. Zhu, F. Oehler, W. Y. Fu, J. T. Griffiths, F. C.-P. Massabuau, M. J. Kappers, T. L. Martin, P. A. J. Bagot, M. P. Moody, and R. A. Oliver, *Appl. Phys. Lett.* **106**, 072104 (2015).
- ²⁴S. Schulz, D. P. Tanner, E. P. O'Reilly, M. A. Caro, D. Sutherland, M. J. Davies, P. Dawson, F. Tang, J. T. Griffiths, F. Oehler, M. J. Kappers, R. A. Oliver, and C. J. Humphreys, *Phys. Rev. B* **92**, 235419 (2015).
- ²⁵R. Kucharski, M. Zając, R. Doradziński, M. Rudziński, R. Kudrawiec, and R. Dwiliński, *Semicond. Sci. Technol.* **27**, 024007 (2012).
- ²⁶R. A. Oliver, F. C.-P. Massabuau, M. J. Kappers, W. A. Phillips, E. J. Thrush, C. C. Tartan, W. E. Blenkhorn, T. J. Badcock, P. Dawson, M. A. Hopkins, D. W. E. Allsopp, and C. J. Humphreys, *Appl. Phys. Lett.* **103**, 141114 (2013).
- ²⁷A. Rosenauer, T. Mehrtens, K. Müller, K. Gries, M. Schowalter, P. V. Satyam, S. Bley, C. Tessarek, D. Hommel, K. Sebald, M. Seyfried, J. Gutowski, A. Avramescu, K. Engl, and S. Lutgen, *Ultramicroscopy* **111**, 1316 (2011).
- ²⁸K. H. Baloch, A. C. Johnston-Peck, K. Kisslinger, E. A. Stach, and S. Gradečak, *Appl. Phys. Lett.* **102**, 191910 (2013).
- ²⁹A. B. Yankovich, A. V. Kvit, X. Li, F. Zhang, V. Avrutin, H. Liu, N. Izyumskaya, Ü. Özgür, B. Van Leer, H. Morkoç, and P. M. Voyles, *Microsc. Microanal.* **20**, 864 (2014).
- ³⁰L. J. Allen, A. J. D'Alfonso, and S. D. Findlay, *Ultramicroscopy* **151**, 11 (2015).
- ³¹R. F. Loane, P. Xu, and J. Silcox, *Acta Crystallogr., Sect. A* **47**, 267 (1991).
- ³²M. Schowalter, A. Rosenauer, J. T. Titantah, and D. Lamoen, *Acta Crystallogr., A* **65**, 227 (2009).
- ³³D. D. Perovic, C. J. Rossouw, and A. Howie, *Ultramicroscopy* **52**, 353 (1993).
- ³⁴V. Grillo, E. Carlino, and F. Glas, *Phys. Rev. B* **77**, 054103 (2008).
- ³⁵S. Plimpton, *J. Comput. Phys.* **117**, 1 (1995).
- ³⁶A. Béré and A. Serra, *Philos. Mag.* **86**, 2159 (2006).
- ³⁷C. J. Rossouw, L. J. Allen, S. D. Findlay, and M. P. Oxley, *Ultramicroscopy* **96**, 299 (2003).
- ³⁸C. Dwyer and J. Etheridge, *Ultramicroscopy* **96**, 343 (2003).
- ³⁹J. M. Lebeau, S. D. Findlay, L. J. Allen, and S. Stemmer, *Ultramicroscopy* **110**, 118 (2010).
- ⁴⁰H. E. K. E. Macarthur, T. J. Pennycook, E. Okunishi, A. J. D'Alfonso, N. R. Lugg, L. J. Allen, and P. D. Nellist, *Ultramicroscopy* **133**, 109 (2013).
- ⁴¹C. J. Rossouw, C. Dwyer, H. Katz-Boon, and J. Etheridge, *Ultramicroscopy* **136**, 216 (2014).
- ⁴²C. Dwyer, R. Erni, and J. Etheridge, *Ultramicroscopy* **110**, 952 (2010).
- ⁴³V. Potin, E. Hahn, A. Rosenauer, D. Gerthsen, B. Kuhn, F. Scholz, A. Dussaigne, B. Damilano, and N. Grandjean, *J. Cryst. Growth* **262**, 145 (2004).
- ⁴⁴L. Hoffmann, H. Bremers, H. Jönen, U. Rossow, M. Schowalter, T. Mehrtens, A. Rosenauer, and A. Hangleiter, *Appl. Phys. Lett.* **102**, 102110 (2013).
- ⁴⁵A. Dussaigne, B. Damilano, N. Grandjean, and J. Massies, in *International Conference on Molecular Beam Epitaxy* (IEEE, 2002), pp. 151–152.
- ⁴⁶M. J. Galtrey, R. A. Oliver, M. J. Kappers, C. J. Humphreys, P. H. Clifton, D. Larson, D. W. Saxey, and A. Cerezo, *J. Appl. Phys.* **104**, 013524 (2008).
- ⁴⁷H. Chen, R. M. Feenstra, J. E. Northrup, J. Neugebauer, and D. W. Greve, *MRS Internet J. Nitride Semicond. Res.* **6**, e11 (2001).
- ⁴⁸Y. Zhao, Q. Yan, C.-Y. Huang, S.-C. Huang, P. Shan Hsu, S. Tanaka, C.-C. Pan, Y. Kawaguchi, K. Fujito, C. G. Van de Walle, J. S. Speck, S. P. DenBaars, S. Nakamura, and D. Feezell, *Appl. Phys. Lett.* **100**, 201108 (2012).
- ⁴⁹N. Sharma, D. Tricker, P. Thomas, Z. Bougrioua, K. Jacobs, J. Cheyns, I. Moerman, T. Thrush, L. Considine, A. Boyd, and C. Humphreys, *J. Cryst. Growth* **230**, 438 (2001).
- ⁵⁰T. Mehrtens, M. Schowalter, D. Tytko, P. Choi, D. Raabe, L. Hoffmann, H. Jönen, U. Rossow, A. Hangleiter, and A. Rosenauer, *Appl. Phys. Lett.* **102**, 132112 (2013).
- ⁵¹M. E. Vickers, M. J. Kappers, T. M. Smeeton, E. J. Thrush, J. S. Barnard, and C. J. Humphreys, *J. Appl. Phys.* **94**, 1565 (2003).
- ⁵²M. E. Vickers, J. L. Hollander, C. McAleese, M. J. Kappers, M. A. Moram, and C. J. Humphreys, *J. Appl. Phys.* **111**, 043502 (2012).
- ⁵³H. Masui, H. Yamada, K. Iso, S. Nakamura, and S. P. DenBaars, *J. Phys. D: Appl. Phys.* **41**, 225104 (2008).
- ⁵⁴K. L. Teo, J. S. Colton, P. Y. Yu, E. R. Weber, M. F. Li, W. Liu, K. Uchida, H. Tokunaga, N. Akutsu, and K. Matsumoto, *Appl. Phys. Lett.* **73**, 1697 (1998).
- ⁵⁵D. Watson-Parris, M. J. Godfrey, P. Dawson, R. A. Oliver, M. J. Galtrey, M. J. Kappers, and C. J. Humphreys, *Phys. Rev. B* **83**, 115321 (2011).
- ⁵⁶F. B. Naranjo, M. A. Sánchez-García, F. Calle, E. Calleja, B. Jenichen, and K. H. Ploog, *Appl. Phys. Lett.* **80**, 231 (2002).
- ⁵⁷D.-P. Nguyen, N. Regnault, R. Ferreira, and G. Bastard, *Solid State Commun.* **130**, 751 (2004).
- ⁵⁸H. Jeong, H. J. Jeong, H. M. Oh, C.-H. Hong, E.-K. Suh, G. Lerondel, and M. S. Jeong, *Sci. Rep.* **5**, 9373 (2015).
- ⁵⁹T.-J. Yang, R. Shivaraman, J. S. Speck, and Y.-R. Wu, *J. Appl. Phys.* **116**, 113104 (2014).